Crystallization of Para-Xylene in Scraped-Surface Crystallizers

Daniel B. Patience and James B. Rawlings
Dept. of Chemical Engineering, University of Wisconsin, Madison, WI 53706

Hazim A. Mohameed
Dept. of Chemical Engineering, Jordan University of Science and Technology, 22110 Irbid, Jordan

Crystallization kinetics of para-xylene in batch pilot-scale scraped-surface crystallizers were determined for commercial crystallization of a xylene mixture currently produced in Amoco plants. Dynamic mass and energy balances, coupled with the dynamic population balance, were used to model the scraped-surface crystallizer. The model assumes that crystal nucleation occurs at the walls of the crystallizer and crystal growth occurs in the bulk. The parameters in the kinetic models were estimated from online measurements of bulk temperature and slurry transmittance. Concentration measurements show that the xylene mixture is always saturated (supersaturation is essentially zero) during all crystallization runs. Therefore, a reduced, two-parameter, high growth rate model was developed to describe these crystallizers. The kinetic parameters were correlated highly for the reduced model. A new batch experiment with an alternative temperature profile was determined that removes the correlation and allows both parameters to be determined uniquely.

Introduction

Xylene mixtures, consisting of ortho-xylene, para-xylene, meta-xylene, and ethyl-benzene, are produced mainly from petroleum. Selected naphtha streams from reformed petroleum are used to produce the xylene mixture. Para-xylene is a base chemical for the production of terephthalic acid (TPA) and dimethylterephthalate (DMT). These products are used for the production of fiber, films, and polyethyleneterephthalate (PET) bottle manufacturing.

Many physical properties of the individual xylene isomers are similar. Consequently, the production of individual xylene isomers of high purity is difficult. Crystallization is one of the practical methods for the commercial production of pure para-xylene. Several commercial crystallization processes have been developed to separate para-xylene from its isomer mixture, often named after the company that applied the process. Among these is the Amoco process (Lammers, 1965; Spiller, 1958; Hoff, 1957), which is studied in this work. Other processes, such as the Chevron, Arco, Phillips and Exxon processes, are described in more detail by Ransley (1984) and Arkenbout (1995). The Amoco process is shown in Figure 1. The Amoco process uses two or more scraped-surface crystallizers (SSCs) in the first stage to bring the temperature of the xylene mixture to the para-xylene/meta-xylene eutectic point. The first-stage crystallization process is followed by a solid-liquid separation process using centrifuges. The cold xylene filtrate (usually called the mother liquor) from the first stage cools the feedstream and is sent to the isomerization process. To achieve the maximum production rate from a certain feedstock, the first-stage mother liquor should contain the eutectic para-xylene/meta-xylene concentration. The solid cake para-xylene crystals and the adherent mother liquor are melted and pumped to the second-stage crystallizer. The product from the second-stage crystallizer is pumped to the final centrifuges. A portion of the second-stage mother liquor is returned to the second-stage crystallizers to control the solids concentration and the remainder is pumped with the feed to the first-stage crystallizers. The cake from the second-stage crystallizer is melted to form the final para-xylene product. This process described in Figure 1, however, is not necessarily practiced commercially today. As the costs

Correspondence concerning this article should be addressed to J. B. Rawlings.

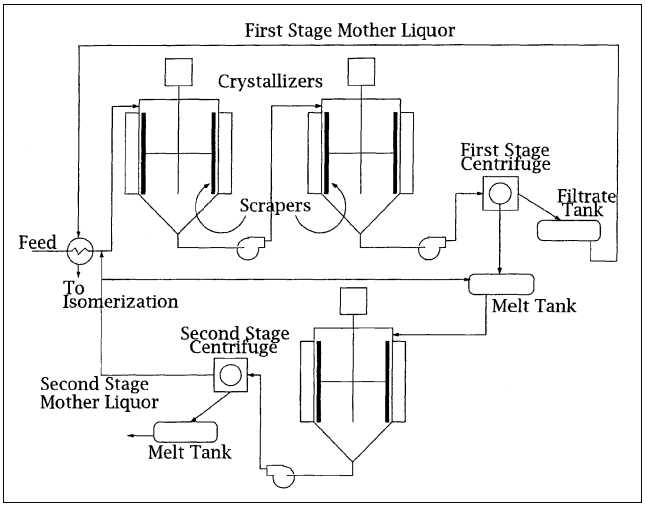

Figure 1. Amoco para-xylene crystallization process.

for melting the cake from the first stage and using second-stage crystallization become higher, process alternatives become attractive. One alternative is to re-slurry the first-stage cake with a higher purity para-xylene stream coming from a later stage of purification (Cannella, 1998).

All the above mentioned crystallization processes use an indirect cooling method and all are based on suspension crystallization from the melt rather than layer crystallization. Recently, a commercialized layer crystallization process from Sulzer Chemtech has been developed to separate para-xylene using heat pump crystallizers. However, the new Sulzer Chemtech technology has a restriction on the feed composition that it should contain more than 80 wt. % para-xylene, compared to the usual feedstock to the first crystallization stage of about 20 to 25 wt. % para-xylene. Therefore, the layer crystallization technique can be augmented to existing separation plants to increase the final para-xylene purity to 99.9 wt. % (Jans and Fischer, 1996).

Pure para-xylene crystals can be separated in one stage since para-xylene forms a eutectic with meta-xylene. However, the separation of the mother liquor from the para-xylene crystals is difficult and is greatly influenced by the crystal-size density, and so the process variables governing nucleation and growth are of importance. Understanding and improving the crystallization process leads to a better solid-liquid separation process. Even with new alternatives such as the re-slurrying step instead of the second-stage crystallizers, controlling the crystal size density from the first stage is still of importance.

The SSC has been treated in the literature as a type of scraped-surface heat exchanger (SSHE) (Härröd, 1986). SSHEs are fitted with blades that continuously scrape the heat exchange surface to minimize fouling and to improve heat-transfer rates. The difference between SSCs and heat exchangers is that a phase change from liquid to solid occurs in the SSC. The formation of the solid layer on the wall of the SSC affects the heat-transfer rate. Scraping the solid layer and transferring solid to the bulk of the crystallizer affects the hydrodynamic and power requirements. Typical examples of the application of SSCs in the chemical industry are the separation of para-xylene from xylene mixtures and the separation of chlorinated benzenes. In the food industry, SSCs are used in the production of ice cream and margarine.

In this work, we first discuss the literature regarding SSCs with phase change on the processing side. Review articles on SSHEs without phase change are provided by Abichandani et al. (1987) and Härröd (1986). Other relevant literature covers the theoretical and empirical models of heat transfer (Trommelen et al., 1971; Örvös et al., 1994; Härröd, 1990), flow patterns and hydrodynamics (Trommelen and Beek, 1971a), residence time distribution (Bott et al., 1968), and power requirements (Trommelen and Beek, 1971b).

de Goede and de Jong (1993) studied heat-transfer issues in a continuous bench-scale (0.07 m outside diameter and 1 m length) SSC for a xylene mixture produced by Exxon. Two scraper speeds were investigated in the turbulent flow regime, 30 and 60 rpm. The experimental data showed that the heat-transfer coefficient depends strongly on the rotational speed of the scrapers. Generation of vortices at high rotational scraper speeds has been confirmed by computer simulation and experimental flow visualization. Ay et al. (1979) reported the heat-transfer coefficient of a SSC operating with a mixture of 60% para-nitroacetophenone and 40% para-nitroethylbenzene. The heat-transfer coefficient has been measured as a function of the slurry density at different scraper speeds. The model assumes that the melt is in equilibrium with the solid crystals and the crystals only form as a layer on the walls of the crystallizer. The model did not include growth and nucleation rate kinetics. Another study by Weisser (1975) used a bench-scale SSC to study the heat transfer inside the crystallizer. The results correlate the Nusselt number as a function of Reynolds and Prandtl numbers and the number of scrapers. The empirical formula takes the phase change into consideration. Nerlich et al. (1981) studied the effect of the operating conditions on mass- and heat-transfer processes in crystallization of para-xylene. A continuous industrial scale SSC of 140 m^3 was used for this study. The linear crystal growth rate was calculated using a steady-state mixed suspension mixed-product removal model. The growth rate was found to depend on the suspension density. Formation of a crystal layer on the walls of the SSC was taken into consideration to calculate the internal heat-transfer coefficient. Russel and Bongers (1997) developed a model for an ice cream SSC (called a freezer in the original article). The model considered the SSC as a series of well-mixed stages using mass and energy balance equations. The model was not presented in the work, but the simulations show good prediction of the product temperature and mechanical dissipation due to shaft rotation and heat transfer.

Crystallization of para-xylene from pure melt or from isomer mixtures has been analyzed in the literature. de Goede and van Rosmalen (1990ab) studied the growth of single para-xylene crystals in a small cell. The growth rate was determined by taking photographs at constant time intervals. They studied the growth rate from pure para-xylene melt and from binary mixtures of 70% para-xylene and 30% other hydrocarbons such as meta-xylene, ortho-xylene, ethylene, benzene, and toluene. They also studied the growth rate in a multicomponent mixture with a freezing point from -20 to -30°C. The proposed growth rate expression considered the heat and mass transfer and surface reaction steps.

Table 1. Physical Properties of Para-Xylene Used in Eq. 1

Component	Freezing Point [K]	Heat of Fusion [$J \cdot mol^{-1}$]	Heat Capacity [$J \cdot mol^{-1} \cdot K^{-1}$]
para-xylene	286.4	17113	24.3

From Mullin (1993).

Solubility data for para-xylene in xylene mixtures are calculated based on the assumption that the xylene mixture behaves as an ideal solution and the crystallized solid phase is pure para-xylene. The presence of nonxylene compounds like toluene is considered to behave similarly to the other xylene compounds (McKay et al., 1966). The experimental data provided by Haddon and Johnson (1964) and Porter and Johnson (1967) show that para-xylene has nonideal behavior and its solubility deviates from the solubility predicted by the correlation based on an ideal solution. Within the studied range of temperatures in the present work, we have found that para-xylene solubility can be predicted by the following equation (Hildebrand et al., 1970)

$$\ln\left(\frac{1}{N}\right) = \frac{\Delta H_f}{RT_m}\left(\frac{T_m}{T} - 1\right) - \frac{\Delta C_p}{R}\left(\frac{T_m}{T} - 1\right) + \frac{\Delta C_p}{R}\ln\left(\frac{T_m}{T}\right) \tag{1}$$

where N is the mol fraction of para-xylene in the mixture at absolute temperature T (K), ΔH_f is the latent heat of fusion ($J \cdot mol^{-1}$), T_m is the melting point (K), ΔC_p is the difference in heat capacities of the solid and the liquid phase ($J \cdot mol^{-1} \cdot K^{-1}$), and R is the gas constant. The physical properties for para-xylene are shown in Table 1, Mullin (1993).

The literature on SSCs can be summarized as follows:

- Heat-transfer issues are the most commonly studied.
- There are a few studies on the growth rate kinetics of para-xylene, but little has been mentioned regarding nucleation kinetics.
- The dynamic population balance approach has not been applied to para-xylene crystallization kinetics.

The objective of this work is to model SSCs incorporating both crystal nucleation and growth kinetics. Crystallization is described in terms of dynamic mass and energy balances, coupled with the dynamic population balance that describes the particle-size density (PSD) of the population of crystals in the continuous phase of a well-mixed heterogeneous system. A nonlinear parameter estimation routine is used to estimate the nucleation rate and growth rate kinetic parameters.

Experimental Apparatus

The experiments are carried out in a pilot plant, 10 gal., nickel-chromium, SSC shown in Figure 2. The SSC has a width to height ratio of 0.25. Scraper blades are mounted on a central shaft and are pressed against the crystallizer's wall. The shaft rotates at a constant speed of 12 rpm.

The alcohol-water coolant mixture passes through the jacket of the crystallizer and has a freezing point below 193 K. A spiral partition wall is inserted in the jacket in order to keep a large flowing speed through the jacket for better heat transfer. Fresh coolant is mixed with part of the outlet jacket stream before returning to the jacket of the crystallizer. Excess coolant is purged from the jacket circuit at the outlet of the jacket. The fresh coolant flow rate coming from the coolant supply is measured and controlled by a Prowirl 70 vortex flowmeter and microprocessor. The crystallizer and piping are thermally insulated. A transmittance measurement is provided by an *in situ* colorimeter probe (Brinkman) that is mounted in the slurry recirculation loop. The incident light from the transmitting light fiber on one side of the tube is projected perpendicular through the flowing slurry. The receiving light fiber (opposite the incident light beam) takes the transmitted light beam and sends it to the colorimeter. The distance the light beam travels through the slurry is 2 mm. Temperature measurement is provided by *in situ* resistance temperature detectors (RTD) installed in the middle (T1) and top (T2) of the crystallizer, the slurry recirculation loop (T3), and the inlet (T4) and outlet (T5) jacket temperatures. A typical temperature-time data set is shown in Figure 3. The difference between the middle temperature and the top temperature is less than 0.1 K and the maximum difference between

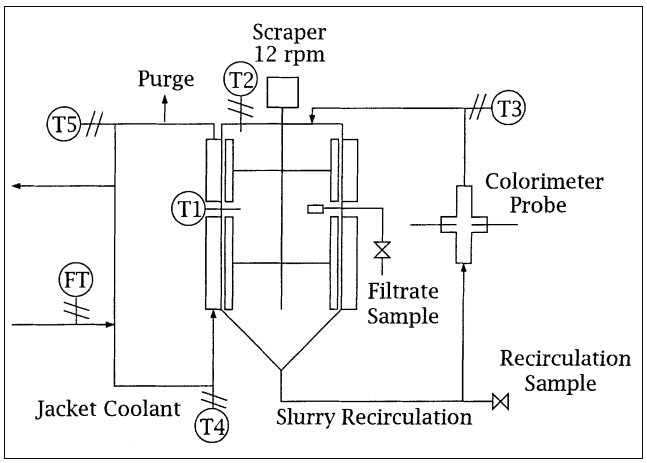

Figure 2. Pilot-plant para-xylene crystallization process.

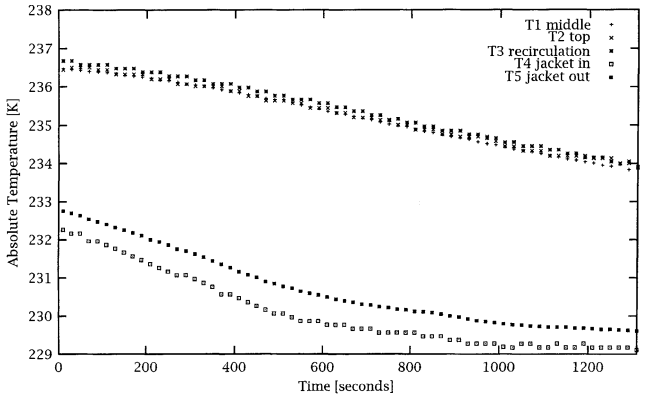

Figure 3. Typical collected temperature data from the pilot-plant scraped-surface crystallizer: run 15.

Cooling rate = 0.11 $K \cdot min^{-1}$.

the middle and recirculation temperature is not more than 0.2 K. Therefore, the temperature is assumed to be homogeneous in the crystallizer and the modeling in this work is based on the middle temperature T1. The small difference between the three temperature measurements T1, T2, and T3 shows good mixing conditions inside the crystallizer. The outlet jacket temperature is warmer than the inlet jacket temperature by 0.4 to 0.8 K. Since the difference is not large, the outlet jacket temperature is accepted to be the jacket temperature in the simulations. The fresh coolant is injected into the jacket circuit at an absolute temperature of approximately 193 K. The absolute temperature of the coolant exit stream is approximately 201 K. The middle temperature T1 inside the crystallizer is controlled by a cascade controller. The master controller uses T1 as a measurement and changes the set point for the inlet coolant temperature to the slave controller. The slave controller uses the inlet jacket temperature as a measurement and manipulates the fresh coolant flow rate coming from a chiller to the jacket circuit.

The crystallization experiments are carried out using a feedstock that has an approximate composition of 25 wt. % para-xylene, 45 wt. % meta-xylene, 18 wt. % ortho-xylene, 8 wt. % ethylbenzene, and 4 wt. % other hydrocarbons. This feedstock has a saturation temperature of approximately 238 K (the temperature at which the crystals are first formed). Toluene concentration is kept at less than 0.7 wt. % for final product purity requirements (de Goede, 1988). Molecular sieves are used to reduce the water content in the feedstock to less than 200 ppm. For safety reasons and to avoid any oxidation of the xylene mixture, an inert nitrogen gas blanket is provided inside the crystallizer and the feed tank. The para-xylene concentrations are measured using gas chromatography (GC). Figure 2 shows where the samples are drawn off. A sampling tube extends through the wall of the crystallizer. A micro-metallic filter is welded to the tube on the inner side of the crystallizer to avoid intake of the solid crystals with mother liquor. A hand pump is attached to the other side where the samples are collected. Samples are taken at the start and at different times during the experiments. Typical concentration data are shown in Figure 4. The equilibrium concentration (solid line) is calculated from Eq. 1.

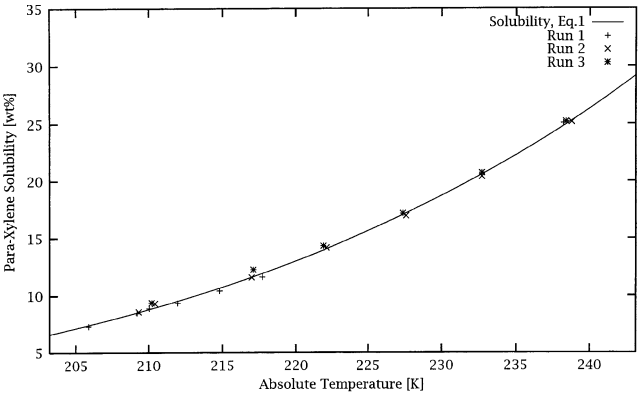

Figure 4. Experimental gas chromatography (GC) measurements (symbols) vs. equilibrium concentration (solid line, Eq. 1) for three different runs.

These concentration data will be used later for model reduction.

All the experiments are done in batch mode where a certain weight of the xylene mixture is introduced to the crystallizer at the beginning of the crystallization run. The crystallization is cooled down to 3 K above the saturation temperature and then the desired cooling ramp is applied. The cooling rate used in this study is 0.11 $K \cdot min^{-1}$ ($0.2°F \cdot min^{-1}$). All the temperatures, the coolant fresh flow rate and the transmittance measurements are recorded and sent to a main computer with a sampling time of 10 s.

Model Formulation and Solution

The PSD of a slurry in a batch SSC is modeled by the population balance equation (PBE) similar to that presented by Miller and Rawlings (1994). The PBE is a partial differential equation in time t and crystal size L

$$\frac{\partial f(L,t)}{\partial t} = -G\frac{\partial f(L,t)}{\partial L} \tag{2}$$

in which $f(L,t)$ is the PSD and G is the size-independent crystal growth rate.

The solution phase concentration in the crystallizer is described by a mass balance of the crystallizing solute, para-xylene

$$\frac{d\hat{C}}{dt} = -3\rho_c k_v hG\int_0^\infty f(L,t)L^2 dL \tag{3}$$

in which $\hat{C}$ is the concentration (mass of para-xylene per total mass of the mother liquor), ρ_c is the crystal density, k_v is the volume shape factor converting L^3 into crystal volume, and h converts solvent mass to slurry volume. For these experiments, the volume shape factor is 1.

The bulk temperature can be predicted from an energy balance on the SSC

$$\rho V C_p\frac{dT}{dt} = -3\Delta H_c\,\rho_c k_v VG\int_0^\infty f(L,t)L^2 dL - UA\left[T - T_j(t)\right] \tag{4}$$

in which T is the bulk temperature, ρ is the slurry density, V is the slurry volume, C_p is the heat capacity of the slurry, ΔH_c is the heat of crystallization which is assumed to be constant, U is the overall heat-transfer coefficient, A is the surface area available for heat transfer, and $T_j(t)$ is the time-dependent outlet jacket temperature. Equation 4 shows that the energy balance is a function of two independent processes: internal heat generation due to crystallization and heat removal by the coolant in the jacket. An average value for U is calculated from the experimental data and found to be 5,085 $W \cdot m^{-2} \cdot K^{-1}$.

The kinetic expressions are taken to be empirical power laws in supersaturation. It is assumed in this model that nucleation is mainly occurring on the wall of the crystallizer due to the high-temperature difference between the coolant and the bulk, while growth occurs in the bulk. Therefore, the

driving force for nucleation is the difference between the bulk concentration and the saturation concentration calculated at the wall temperature. It is assumed that the wall temperature is the same as the jacket temperature, because the values of the heat conductivities of the material of construction and the para-xylene layer on the wall are 12.75 $W \cdot m^{-1} \cdot K^{-1}$ and 0.29 $W \cdot m^{-1} \cdot K^{-1}$, respectively. Also, the resistance through the 8 mm thick wall is negligible compared to the heat transfer through the bulk. The para-xylene forms a uniform layer on the wall with an average thickness of 0.5 mm. This suggests that the wall resistance can be neglected and the wall temperature can be taken as the jacket temperature. The nucleation kinetics are described by the following empirical expression

$$B = k_b \left\{ \frac{\hat{C} - \hat{C}_{\text{sat}}[T_j(t)]}{\hat{C}_{\text{sat}}[T_j(t)]} \right\}^b \tag{5}$$

The driving force for the growth rate is the difference between the bulk concentration and the saturation concentration calculated at the bulk temperature. The growth kinetics are described by

$$G = k_g \left\{ \frac{\hat{C} - \hat{C}_{\text{sat}}[T(t)]}{\hat{C}_{\text{sat}}[T(t)]} \right\}^g \tag{6}$$

The parameters k_b, b, k_g, and g are inferred from experimental data.

The Beer-Lambert law is used to relate the transmittance measurement to the second moment of the PSD

$$\frac{I}{I_0} = \exp\left[-\frac{l k_a}{2} \int_0^\infty f(L,t) L^2 dL \right] \tag{7}$$

I is the intensity of the light transmitted through the slurry, I_0 is the intensity of the incident light, l is the beam length (m), and k_a is the area shape factor. For these experiments, the area shape factor is 6.

The zero-size boundary condition for Eq. 2 is defined as

$$f(0,t) = \frac{B}{G|_{L=0}} \tag{8}$$

The PBE Eq. 2 is solved using the method of moments. Matthews (1997) provides a complete description of the batch crystallizer model. The ith moment of the PSD is defined as

$$\mu_i = \int_0^\infty f(L,t) L^i dL \tag{9}$$

The general batch crystallizer model Eqs. 2, 3 and 4 require the first four moments to be determined

$$\frac{d\mu_0}{dt} = B \qquad \text{for } i = 0 \tag{10a}$$

$$\frac{d\mu_i}{dt} = iG\mu_{i-1} \qquad \text{for } i = 1,2,3 \tag{10b}$$

and the integral terms in the mass and energy balances (Eqs. 3 and 4), and the Beer-Lambert law (Eq. 7) are replaced by μ_2. The initial conditions for moments, mass and energy balances, respectively, are

$$\mu_i(t) = 0, \quad t = 0 \quad \text{for } i = 0,1,2,3 \tag{11a}$$

$$\hat{C}(t) = \hat{C}_0, \quad t = 0 \tag{11b}$$

$$T(t) = T_0, \quad t = 0 \tag{11c}$$

The zeroth and first moments are the total number of particles and their total length, respectively. The second and third moments are proportional to the total crystal surface area and volume, respectively.

Initial Estimation of Kinetic Parameters

The kinetic parameters in Eqs. 5 and 6 are estimated from experimental data collected for the para-xylene system by posing a nonlinear program (NLP) with a maximum likelihood objective function (Matthews and Rawlings, 1998; Miller and Rawlings, 1994). The following assumptions are considered about the prediction errors:

- The prediction errors are Normally distributed with zero mean and covariance matrix $\boldsymbol{V}$.
- Prediction errors corresponding to different sample times are uncorrelated.
- Prediction errors corresponding to the m different measurement types are uncorrelated.
- The prediction errors are homoscedastic (error variance is independent of the magnitude of the measured variable).

Under these assumptions, it can be shown that the maximum likelihood method is equivalent to the minimization of

$$\Phi_{be} = \sum_{k=1}^{m} (n_k + 1) \ln\left[\sum_{i=1}^{n_k} e_{ik}^2(\boldsymbol{\theta}) \right] \tag{12}$$

where n_k is the number of measurements of the kth type and e_{ik} is the prediction error of the ith measurement of the kth type. Given the optimal model parameters $\hat{\boldsymbol{\theta}}$ the maximum-density estimate of the prediction variance for the kth measurement type $\hat{\sigma}_k^2$ is

$$\hat{\sigma}_k^2 = \frac{\sum_{i=1}^{n_k} e_{ik}^2(\hat{\boldsymbol{\theta}})}{n_k + 1} \tag{13}$$

An approximation of the spread of the posterior density may be obtained by assuming that the model can be represented as linear in the parameters in the vicinity of the model estimates. Linearization allows the determination of the Hessian, $\boldsymbol{H}_{\theta\theta}$ which describes the curvature of the distribution about the mode.

The confidence intervals for the model parameters may be determined according to

$$\theta_i \approx \hat{\theta}_i \pm \sqrt{\chi_p^2(\alpha) \boldsymbol{H}_{\theta\theta}^{-1}(i,i)} \tag{14}$$

where $\boldsymbol{H}_{\theta\theta}^{-1}(i,i)$ is i, i element of $H_{\theta\theta}^{-1}$. The linear 95% confidence intervals are calculated according to Eq. 14 with α

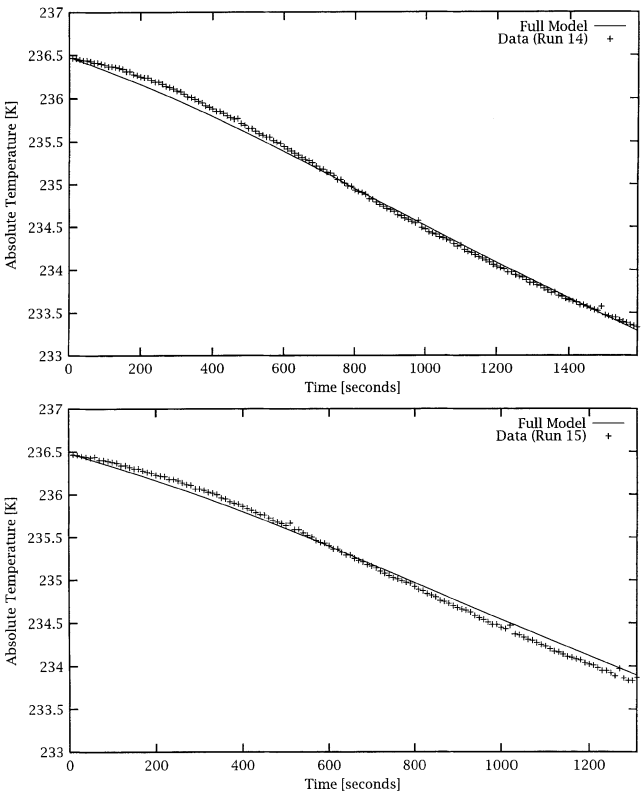

Figure 5. Temperature profile and full model fit for runs 14 and 15.

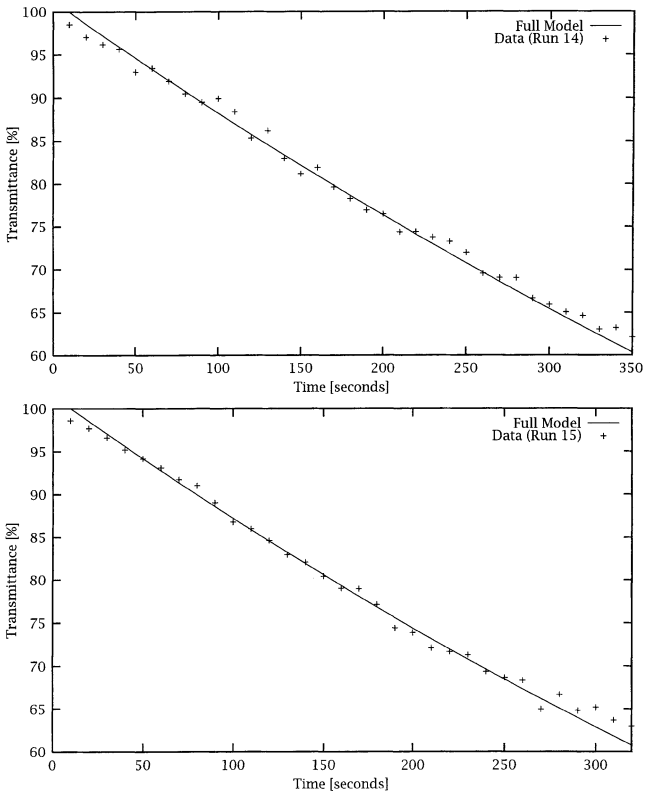

Figure 6. Transmittance profile and full model fit for runs 14 and 15.

equal to 0.025. More detailed presentations of Bayesian inference of parameters from data are given by Stewart et al. (1992, 1998) and Box and Tiao (1973).

The kinetic parameters given in Eqs. 5 and 6 are estimated from experimental data for xylene mixtures. The parameter vector of the model has the form

$$\boldsymbol{\theta} = \begin{bmatrix} k_g & : & \text{growth rate constant} \\ g & : & \text{growth rate order} \\ k_b & : & \text{nucleation rate constant} \\ b & : & \text{nucleation rate order} \end{bmatrix} \tag{15}$$

The sequential quadratic programming code NPSOL (Gill et al., 1986) was used to solve this unconstrained optimization problem.

The results for two runs (14 and 15) are presented in Figures 5 and 6. The parameter estimates and their 95% confidence intervals are presented in Table 2. The temperature data are reasonably well described by the model, which underpredicts slightly at early times and overpredicts slightly for latter times. The transmittance data are also well described by the model in the region of single light scattering (transmittance >74%). The parameter values are physically realistic. Typically, in crystallization systems, b and g are of the order of 0 to 3 whereas the rate constants k_b and k_g are only known to be positive. Second derivatives for calculating the Hessian at the local optimum are difficult to obtain, because the objective function is essentially flat in at least one direction of the parameter space. The Gaussian approximation to the Hessian is used instead of second-order finite differences and converges to a solution using a step size of 10^{-3} to 10^{-6}. The size of the confidence intervals suggests that the model is overparameterized or there are insufficient data and/or measurement types to identify uniquely the four parameters. Thus, revisions of the model are required.

Model Reduction: High Growth Rate Limit

The concentration measurements in Figure 4 show that the bulk concentration of para-xylene is within GC experimental error of the equilibrium concentration during the entire crystallization run. We assume, therefore, the para-xylene growth rate is large and rapid growth depletes any supersaturation in the bulk of the crystallizer almost instantly and deposits the para-xylene solid on the available crystals in the bulk and nuclei scraped from the walls. We do not expect to be able to

Table 2. Parameter Estimates and Approximate 95% Confidence Intervals from Temperature and Transmittance Measured for Runs 14 and 15

	$\ln(k_g)$	g	$\ln(k_b)$	b
Estimate (Run 14)	−2.85	0.68	9.75	0.05
Interval	±297	±37	±12	±6
Estimate (Run 15)	3.61	0.80	10.80	0.44
Interval	±1000	±113	±14	±7

operate this class of crystallizer outside of this high growth regime.

In order to reduce the model and remove the large parameter k_g that is not estimable from these data, we take the limit $k_g \to \infty$ and we know $C \to C_{\text{sat}}(T)$, which is verified in Figure 4. Given

$$\hat{C} = \hat{C}_{\text{sat}}(T) \tag{16}$$

and from Eq. 3, we have

$$\frac{d\hat{C}}{dt} = \frac{d\hat{C}_{\text{sat}}(T)}{dt} = -3\rho_c k_v h G \int_0^\infty f(L,t) L^2 dL \tag{17}$$

The derivative of the saturation concentration with respect to temperature can be found analytically from Eq. 1 and $C_{\text{sat}} = 100N$, in which N is the mol fraction of para-xylene. Applying the chain rule and rearranging Eq. 17 results in the reduced growth rate expression

$$G = \frac{-1}{3h\rho_s k_v}\left(\frac{1}{\mu_2}\right)\left[\frac{d\hat{C}_{\text{sat}}(T)}{dT}\right]\left(\frac{dT}{dt}\right) \tag{18}$$

where μ_2 is the second moment of the PSD. Randolph and Larson (1988) provide the steady-state version of the high growth limit, which is discussed in the Appendix. Substituting Eq. 18 into Eq. 4 results in

$$\rho V C_p \frac{dT}{dt} = \frac{-UA\left[T - T_j(t)\right]}{1 - \left(\frac{\Delta H_c}{\rho C_p h}\right)\left[\frac{d\hat{C}_{\text{sat}}(T)}{dT}\right]} \tag{19}$$

Substitution of Eq. 18 into Eqs. 10a and 10b results in the following expressions for the moments

$$\frac{d\mu_0}{dt} = B \tag{20}$$

$$\frac{d\mu_1}{dt} = -\frac{1}{3h\rho_c k_v}\left(\frac{\mu_0}{\mu_2}\right)\left[\frac{d\hat{C}_{\text{sat}}(T)}{dT}\right]\left(\frac{dT}{dt}\right) \tag{21}$$

$$\frac{d\mu_2}{dt} = -\frac{2}{3h\rho_c k_v}\left(\frac{\mu_1}{\mu_2}\right)\left[\frac{d\hat{C}_{\text{sat}}(T)}{dT}\right]\left(\frac{dT}{dt}\right) \tag{22}$$

$$\frac{d\mu_3}{dt} = -\frac{1}{h\rho_c k_v}\left[\frac{d\hat{C}_{\text{sat}}(T)}{dT}\right]\left(\frac{dT}{dt}\right) \tag{23}$$

The initial derivatives for the first and second moments in the reduced model are undefined because $\mu_i(0) = 0$. Instead, values of the initial rate of change of first and second moments are evaluated analytically by taking the limit as step-size tends to zero in an implicit Euler approximation resulting in

$$\left.\frac{d\mu_0}{dt}\right|_{t=0} = B \tag{24}$$

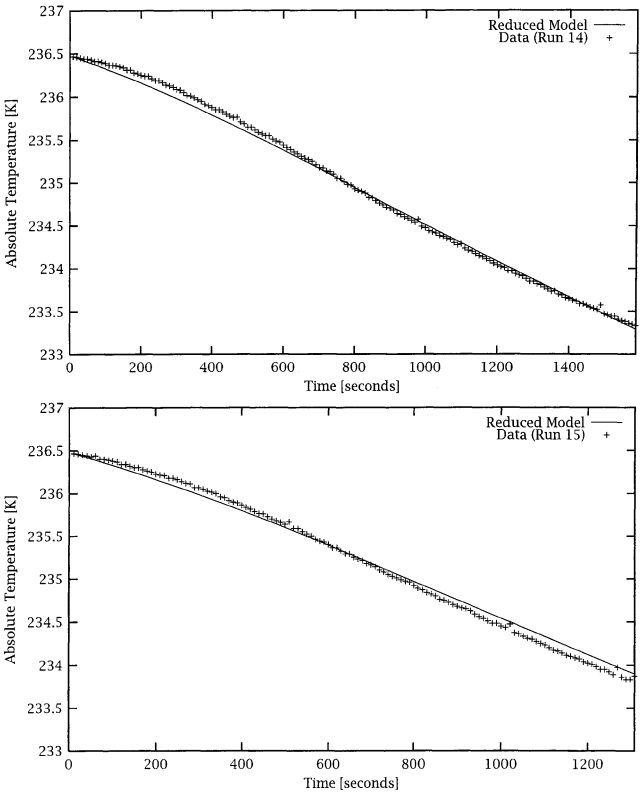

Figure 7. Temperature profile and reduced model fit for runs 14 and 15.

$$\left.\frac{d\mu_1}{dt}\right|_{t=0} = \left\{\frac{-(B)^2}{6h\rho_c k_v}\left[\frac{d\hat{C}_{\text{sat}}(T)}{dT}\right]\left(\frac{dT}{dt}\right)\Big|_{t=0}\right\}^{1/3} \tag{25}$$

$$\left.\frac{d\mu_2}{dt}\right|_{t=0} = \left\{\frac{-\sqrt{2B}}{3h\rho_c k_v}\left[\frac{d\hat{C}_{\text{sat}}(T)}{dT}\right]\left(\frac{dT}{dt}\right)\Big|_{t=0}\right\}^{2/3} \tag{26}$$

and $(dT/dt)|_{t=0}$ can be evaluated from Eq. 19. The nucleation rate does not change in the reduced model and still can be calculated from Eq. 5. The growth rate is calculated from Eq. 18. In the reduced model, only the nucleation rate parameters k_b and b are estimated

$$\boldsymbol{\theta} = \begin{bmatrix} k_b & : & \text{nucleation rate constant} \\ b & : & \text{nucleation rate order} \end{bmatrix} \tag{27}$$

The results for runs 14 and 15 using the reduced model are presented in Figures 7 and 8. The reduced model parameter estimates and 95% confidence intervals are presented in Table 3. The fit to the experimental data for the reduced model is essentially identical to the fit for the full model verifying the accuracy of the reduced model for this crystallizer.

Analysis of Confidence Regions for the Reduced Model

The confidence regions for the reduced model for runs 14 and 15 are shown in Figure 9. Figure 10 shows the objective

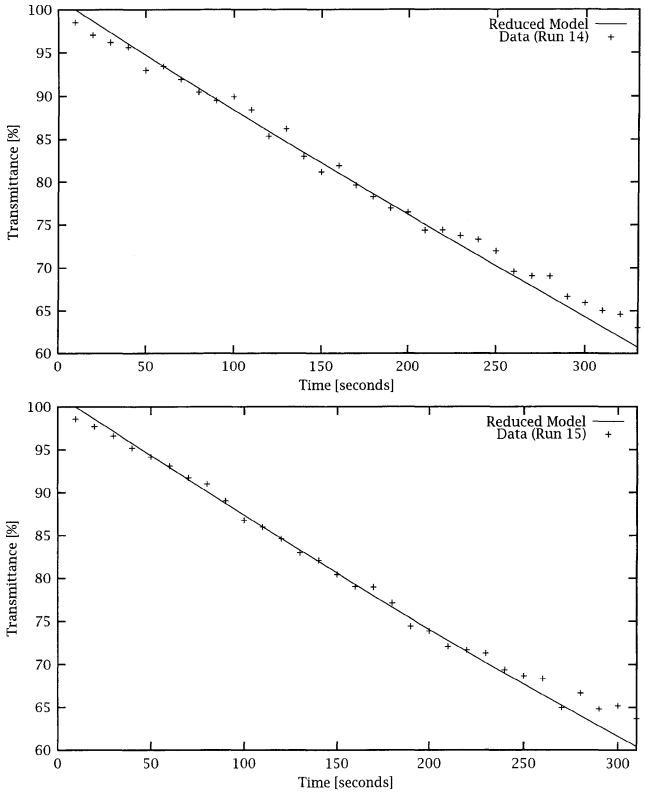

Figure 8. Transmittance profile and reduced model fit for runs 14 and 15.

function near the respective optima. The objective surface remains essentially flat in one direction and is steep in the orthogonal direction. The shapes of the confidence regions show that the parameters k_b and b are highly correlated. Again, the size of the intervals of the parameters in Table 3 and the confidence region suggest that either further model revisions are required or a new experimental design is required.

Consider the high values for the nucleation rate k_b in Table 3 and the supersaturation at the wall shown in Figure 11. The value for the supersaturation ratio at the wall is small and does not change significantly throughout the run and is almost identical for both runs 14 and 15. Taking the product of the supersaturation ratio raised to the power of b and a high

Table 3. Parameter Estimates and Approximate 95% Confidence Intervals from Temperature and Transmittance Measured for Runs 14 and 15 and Simultaneous Fit of Simulated Data and Run 15 Using Reduced Model

	$\ln(k_b)$	b
Estimate (Run 14)	24.99	7.80
Interval	±45	±23
Estimate (Run 15)	21.71	5.94
Interval	±16	±8
Estimate (Simulated and Run 15)	10.66	0.36
Interval	±0.10	±0.06

Confidence regions are summarized in Figures 9 and 14.

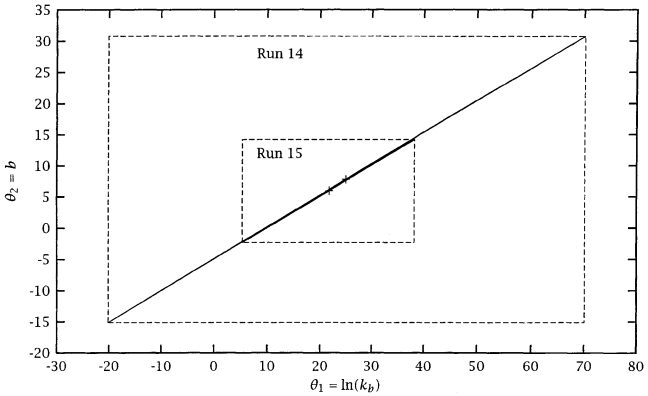

Figure 9. Parameter approximate 95% inference regions for runs 14 and 15 data using the reduced model.

rate constant results in a relatively constant value for the nucleation rate B. Consider the expression for the rate of nucleation

$$B = \exp[\ln(k_b)]S_w^b = \exp(\theta_1)S_w^{\theta_2} \tag{28}$$

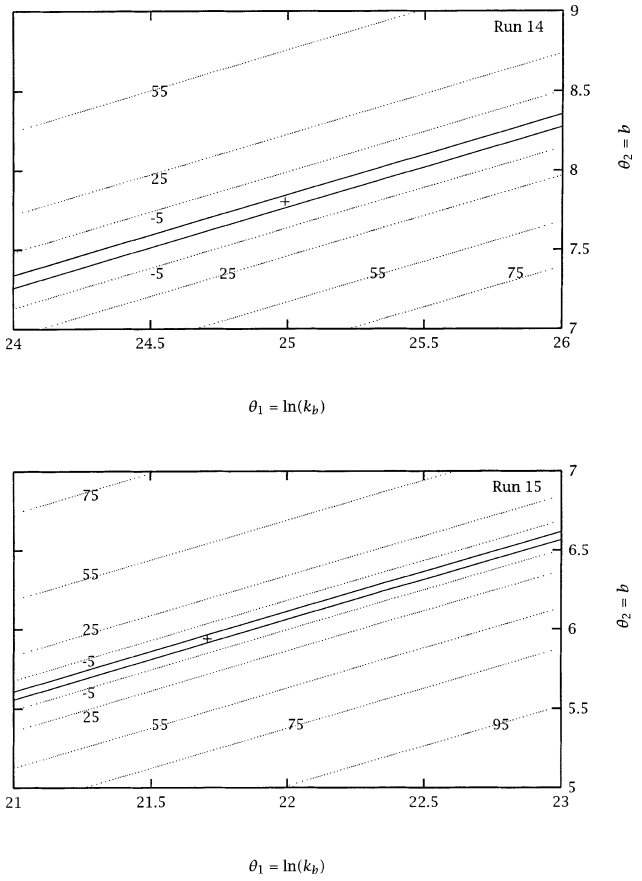

Figure 10. Objective function (Φ_{be}) contours and a portion of the 95% inference regions for runs 14 and 15 data.

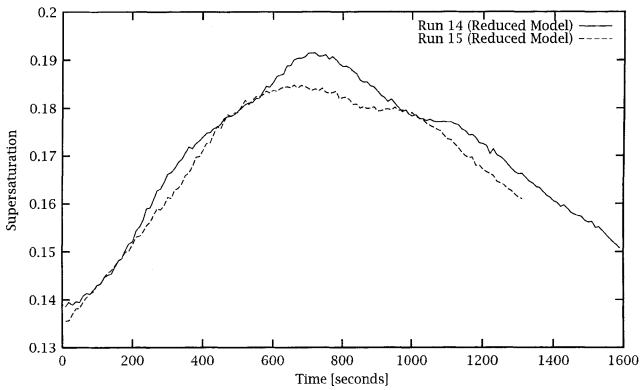

Figure 11. Supersaturation profiles at the wall predicted using the reduced model for runs 14 and 15.

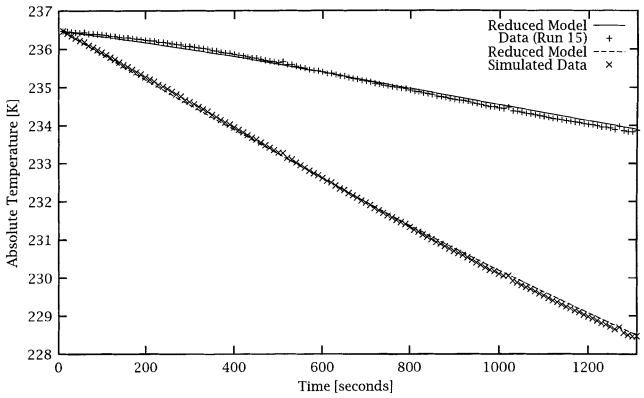

Figure 12. Temperature profile and reduced model fit for run 15 and simulated data.

in which $S_w = \{\hat{C} - \hat{C}_{\text{sat}}[T_j(t)]\}/\hat{C}_{\text{sat}}[T_j(t)]$. For a truly constant nucleation rate experiment, the correlation would be

$$dB = B\left[d\theta_1 + \ln(S_w)d\theta_2\right] = 0 \tag{29}$$

so

$$\frac{d\theta_2}{d\theta_1} = \frac{-1}{\ln(S_w)} \tag{30}$$

Equation 30 is the value of the slope of the line that results from the limit of the narrow ellipse as it becomes a line for correlated parameters with a correlation coefficient of 1.0. The value of the slope is calculated from the intervals from Figure 9 and is compared with the predictions of the supersaturation at the wall for both runs 14 and 15 in Figure 11 and Eq. 30. The values for the slopes of the ellipses obtained from the inference regions for the reduced model for runs 14 and 15 are 0.51 and 0.50, respectively. The values for Eq. 30 from the model fits for runs 14 and 15 are both 0.56 and are close to the values from the ellipses. We conclude that the experiments were conducted with an approximately constant nucleation rate and that is the cause of the parameter correlation and is, therefore, not an informative experimental design.

Experimental Design

There are two options in which one can eliminate the parameter correlation. The first approach would be to make the transmittance data more informative. In the high growth regime, the parameters k_b and b only affect the transmittance predictions and the temperature predictions are unaffected. If a single run is required to uniquely identify k_b and b, then the supersaturation must be significantly varied with time during the run. The experiment would require that the inlet jacket temperature slowly decrease from its initial temperature of approximately 232 K and, then, while transmittance is still greater than 74%, a rapid decrease to a lower final temperature would create a large supersaturation at the wall.

A second and simpler approach is to use two experiments at constant but different supersaturations. The data from runs 14 and 15 and a second experiment in which the supersaturation at the wall is different from the supersaturation at the walls for runs 14 and 15 can be used to provide experiments with varied supersaturations. A large supersaturation at the wall can be generated, for example, by stepping the inlet jacket temperature to its final temperature at the beginning of the run. Simulated data of the crystallizer temperature and transmittance responses are created by using a set of parameters in the confidence region in Figure 9, namely $\ln(k_b) = 10.74$ and $b = 0.41$, and an inlet jacket temperature of 220 K. The temperature and transmittance responses for the simulated data along with the simultaneous fit from run 15 are shown in Figures 12 and 13. Notice that only few transmittance points can be used for parameter estimation on these rapid cooling profile experiments. The step in the inlet jacket temperature results in a more rapid decrease in the crystallizer temperature compared to run 15. The large supersaturation created at the wall generates many nuclei quickly and so the transmittance profile is steeper than the transmittance profile for run 15.

The parameter estimation routine converged to a local optimum with parameters $\ln(k_b) = 10.66 \pm 0.10$ and $b = 0.36 \pm$

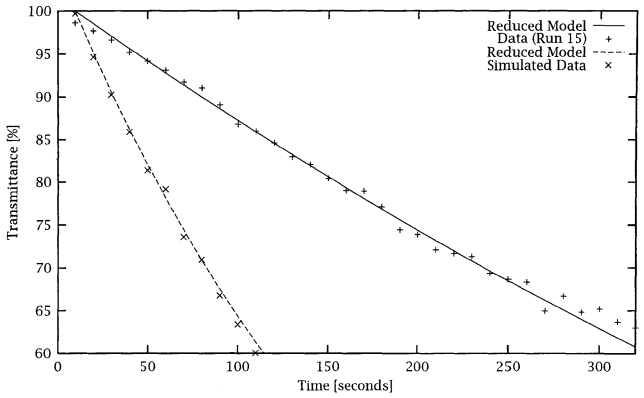

Figure 13. Transmittance profile and reduced model fit for run 15 and simulated data.

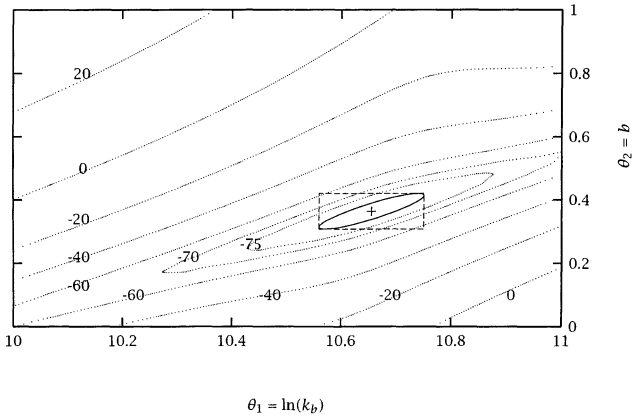

Figure 14. Objective function (Φ_{be}) contours and the 95% inference region for run 15 and simulated data.

0.06. The confidence region and objective surface are shown in Figure 14. The original parameters that generated the simulated data are contained in the linear 95% confidence region. The objective surface shows that the two parameters in the reduced model are much less correlated when two experiments run with significantly different supersaturations are used for parameter estimation.

Conclusions

This article has shown that the predictions of the identified crystallizer models show good agreement with the temperature and light transmittance measurements for crystallization of para-xylene in a batch pilot-scale SSC, assuming nucleation occurs at the wall of the crystallizer, and growth occurs in the bulk. The data show that the para-xylene crystallization system is a high-growth rate process and the bulk supersaturation is essentially zero at all conditions. Therefore, the growth rate constant is assumed large and a reduced model is derived. The nucleation order and the rate constant are the only adjustable parameters in the reduced model. Good agreement with all the data was also obtained with the reduced model, but the reduced model's two parameters remain correlated. The correlation between the nucleation order and rate constant is attributed to the near constant nucleation rate in the available experiments. The parameters can be largely decoupled and determined precisely in a single experiment if data can be collected, while the supersaturation at the wall is time-varying. Alternatively, repeated experiments at constant but differing values of supersaturation can be used. Given the available Amoco experiments and an additional experiment with a step to a low inlet jacket temperature, simulated data show that the parameters are decoupled. It is recommended that this temperature profile be implemented in subsequent parameter estimation studies.

Alternative models can, of course, describe the nucleation kinetics in the crystallizer. Using the data in this study, statistical model discrimination techniques could be used to discriminate between rival models, such as primary vs. secondary nucleation models. This topic could be the focus of further research to understand the crystallization mechanism occurring in an industrial SSC.

Acknowledgments

Financial support from Amoco Chemical Company is gratefully acknowledged. Thanks also to Scott A. Roberts, Richard Wilsak, and Michael J. Liebman for their technical support. Special thanks to D. B. Comstock for his enthusiasm in conducting the experiments on the pilot plant.

Literature Cited

Abichandani, H., S. Sarma, and D. Heldman, "Hydrodynamics and Heat Transfer in Liquid Full Scraped Heat Exchangers—A Review," *J. Food Proc. Eng*., **9**, 121 (1987).

Arkenbout, G. F., *Melt Crystallization Technology*, Technomic, Basel (1995).

Ay, P., H. Wenzlau, and K. Gramlich, "Zur Modellierung des Wärme- und Stofftransport in Kratzkühlerkristallisatoren," *Chemische Technik*, **31**, 341 (1979).

Bott, T., S. Azoory, and K. Porter, "Scraped-Surface Heat Exchangers. Part I: Hold-up and Residence Time Studies," *Trans. Inst. Chem. Eng*., **46**, T33 (1968).

Box, G. E. P., and G. C. Tiao, *Bayesian Inference in Statistical Analysis*, 1st ed., Addison-Wesley, Reading, MA (1973).

Cannella, W. J., "Xylenes and Ethylbenzene," *Encyclopedia of Chemical Technology*, Wiley, New York (1998).

de Goede, R., "Crystallization of Paraxylene with Scraped Heat Exchangers," PhD Thesis, TU Delft (1988).

de Goede, R., and E. de Jong, "Heat Transfer Properties of a Scraped-Surface Heat Exchanger in the Turbulent Flow Region," *Chem. Eng. Sci.,* **48**, 1393 (1993).

de Goede, R., and G. van Rosmalen, "Crystal Growth Phenomena of Para Xylene Crystals," *J. Cryst. Growth*, **104**, 399 (1990a).

de Goede, R., and G. van Rosmalen, "Modeling of Crystal Growth Kinetics: A Simple but Illustrative Approach," *J. Cryst. Growth*, **104**, 392 (1990b).

Gill, P. E., W. Murray, M. A. Saunders, and M. H. Wright, "User's Guide for SOL/NPSOL (Version 4.0): A Fortran Package for Nonlinear Programming," Technical report SOL 86-2, Technical report, System Optimization Laboratory, Dept. of Operations Research, Stanford University (1986).

Haddon, W. F., and J. F. Johnson, "Solubility Data for *p*-Xylene," *J. Chem. Eng. Data*, **9**, 158 (1964).

Härröd, M., "Scraped Surface Heat Exchangers," *J. Food Proc. Eng*., **9**, 1 (1986).

Härröd, M., "Modeling of Laminar Heat Transfer in a Scraped Surface Heat Exchanger," *J. Food Proc. Eng*., **13**, 59 (1990).

Hildebrand, J., J. Prausnitz, and R. Scott, *Regular and Related Solutions*, van Nostrand Reinhold Company, New York (1970).

Hoff, M. C., "Separation of Recovery of Xylene Mixtures," U.S. Patents No. 2,777,888, to Standard Oil Company (1957).

Jans, B., and O. Fischer, "Die Idee mit der Wärmepumpe," *Sulzer Tech. Rev*., **4**, 39 (1996).

Lammers, G. C., "Process for the Recovery of Para-xylene," U.S. Patent No. 3,177,265, to Standard Oil Company (1965).

Matthews, H. B., "Model Identification and Control of Batch Crystallization for an Industrial Chemical System," PhD Thesis, Univ. of Wisconsin-Madison (1997).

Matthews, H. B., and J. B. Rawlings, "Batch Crystallization of a Photochemical: Modeling, Control and Filtration," *AIChE J*., **44**, 1119 (1998).

McKay, D., G. H. Dale, and D. C. Tabler, "Para-Xylene via Fractional Crystallization," *Chem. Eng. Prog*., **62**, 104 (1966).

Miller, S. M., and J. B. Rawlings, "Model Identification and Control Strategies for Batch Cooling Crystallizers," *AIChE J*., **40**, 1312 (1994).

Mullin, J. W., *Crystallization*, 3rd ed., Butterworth, London (1993).

Nerlich, M., G. Wünsch, and K. Schmok, "Der Stoff- und Wärmeübergang in einem industriellen Kratzkühlerkristallisator," *Freib. Forsch.-H*., **A644**, 37 (1981).

Örvös, M., T. Balazs, K. F. Both, and I. Csury, "Investigation of Heat Transfer Conditions in a Scraped-Surface Heat Exchanger," *Periodica Polytechnic Ser. Mech. Eng*., **38**, 123 (1994).

Porter, R. S., and J. F. Johnson, "Extended Xylene Solubility Studies," *J. Chem. Eng. Data*, **12**, 392 (1967).

Randolph, A. D., and M. A. Larson, *Theory of Particulate Processes*, 2nd ed., Academic Press, San Diego, (1988).
Ransley, D. L., "Xylenes and Ethylbenzene," *Encyclopedia of Chemical Technology*, Wiley, New York (1984).
Russel, A., and P. Bongers, "Predictions of Process Conditions within an Ice Cream Freezer," *INTER-EIS' 97: Int. ZDS-Seminar* (1997).
Spiller, C. A., "Paraxylene Purification System," U.S. Patents No. 2,866,833, Standard Oil Co. (1958).
Stewart, W. E., M. Caracotsios, and J. P. Sørensen, "Parameter Estimation from Multiresponse Data," *AIChE J*., **38**, 641 (1992).
Stewart, W. E., Y. Shon, and G. E. P. Box, "Discrimination and Goodness of Fit of Multiresponse Mechanistic Models," *AIChE J*., **44**, 1404 (1998).
Trommelen, A., and W. Beek, "Flow Phenomena in a Scraped-Surface Heat Exchanger (Votator-Type)," *Chem. Eng. Sci*., **26**, 1933 (1971a).
Trommelen, A., and W. Beek, "The Mechanism of Power Consumption in a Votator-Type Scraped-Surface Heat Exchanger," *Chem. Eng. Sci*., **26**, 1977 (1971b).
Trommelen, A., W. Beek, and H. van de Westelaken, "The Mechanism of Heat Transfer in a Votator-Type Scraped-Surface Heat Exchanger," *Chem. Eng. Sci*., **26**, 1987 (1971).
Weisser, H., "Der Wärmeübergang im Kratzkühler bei Teilweiser Phasenänderung," *Chemie-Ing.-Techn*., **47**(2), 73 (1975).

Appendix: High Growth Limits for MSMPRs

Randolph and Larson (1988) discuss mixed suspension, mixed product removal (MSMPR) systems in which the exit concentration approaches $\hat{C}_{\text{sat}}$ and the per pass yield is independent of throughput, named "class II" systems. The authors assume constant temperature and show that the growth rate for this particular system is inversely proportional to the surface area of crystals in suspension. Here we show that the reduced model in the high growth limit in this study is a more general form and does not necessarily need the constant temperature assumption.

For the continuous case, Eq. 17 has the additional terms for the inlet and exit streams

$$\frac{d\hat{C}}{dt} = \frac{d\hat{C}_{\text{sat}}(T)}{dt} = \frac{\hat{C}_{\text{in}}}{\tau} - \frac{\hat{C}_{\text{sat}}}{\tau} - 3\rho_c k_v h G \int_0^\infty f(L,t) L^2 dL \tag{A1}$$

Similar inlet and exit temperature terms are added to Eq. 19 for the energy balance. Rearranging Eq. A1 for growth rate and noting the conversion between volume and area shape factor $6k_v = k_a$

$$G = \frac{2\left\{ \dfrac{d\hat{C}_{\text{sat}}(T)}{dt} - \left[\dfrac{\hat{C}_{\text{in}} - \hat{C}_{\text{sat}}}{\tau} \right] \right\}}{-\rho_c k_a h \mu_2} \tag{A2}$$

Assuming constant temperature so $d\hat{C}_{\text{sat}}/dt = 0$, Eq. A2 becomes Eq. 4.5-3 in Randolph and Larson (1988).

Manuscript received Aug. 26, 2000, and revision received June 11, 2001.